Ensemble Modeling of Successive Halo CMEs:
A Case Study

C.O. Lee[1] · C.N. Arge[2] · D. Odstrcil[3] · G. Millward[4] ·
V. Pizzo[4] · N. Lugaz[5]

Abstract The Wang–Sheeley–Arge (WSA)–Enlil cone modeling system is used for making routine arrival-time forecasts of Earth-directed halo coronal mass ejections (CMEs), since they typically produce the most geoeffective events. A major objective of this work is to better understand the sensitivity of the WSA–Enlil modeling results to input model parameters and how these parameters contribute to the overall model uncertainty and performance. In this study, ensemble-modeling results for a succession of three halo CME events that occurred on 2 – 4 August 2011 are presented. We investigate the sensitivity of the modeled CME arrival times to small variations in the input-cone properties by creating ensemble sets of numerical simulations for each CME event, based on multiple sets of cone parameters. We find that the accuracy of the modeled CME arrival times not only depends on the small variations to the initial input geometry, but also on the reliable specification of the background solar wind, which is driven by the input maps of the photospheric magnetic field. The accuracy in the arrival-time predictions also depends on whether the cone parameters for all three CMEs are specified in a single WSA–Enlil simulation. The inclusion or exclusion of one or two of the preceding CMEs affects the solar-wind conditions through which the succeeding CME propagates. Although the accuracy of the modeled arrival times is sensitive to the input maps that are used to drive the background solar wind, the spread in the modeling ensemble remains mostly unchanged when different input maps are used.

✉ C.O. Lee
clee@ssl.berkeley.edu

1 Space Sciences Laboratory, University of California, Berkeley, CA, USA

2 Air Force Research Laboratory/Space Vehicles Directorate, Kirtland Air Force Base, NM, USA

3 George Mason University, Fairfax, VA, USA

4 NOAA Space Weather Prediction Center, Boulder, CO, USA

5 Space Science Center and Department of Physics, University of New Hampshire, Durham, NH, USA

1. Introduction

Previously, we presented an example of how the sensitivity of 3D numerical magnetohydrodynamical (MHD) results can be assessed from the Wang–Sheeley–Arge (WSA)–Enlil model (Arge and Pizzo, 2000; Arge *et al.*, 2003, 2004; Odstrcil, 2003) to the input-cone geometry for an Earth-directed halo coronal mass ejection (CME) event (Lee *et al.*, 2013b). A modeling ensemble was created from multiple sets of input parameters obtained using a cone-fitting tool together with realistic ranges for the angular width and leading-edge distance estimated from the *Solar TErrestrial RElations Observatory* (STEREO: Kaiser, 2005) observations over the solar limb. Our results highlighted an important cautionary point: the accuracy of the modeled arrival times depends not only on the input-cone CME geometry, but also on the accuracy of the modeled background solar wind, particularly during the several days leading up to the arrival of the CME disturbance at Earth.

As a follow-up to Lee *et al.* (2013b) and to expand upon the preliminary results presented by Lee *et al.* (2013a), we i) continue our assessment of the factors that contribute to the variation in the ensemble spread of the modeled CME shock-arrival times to 1 AU and ii) explore the predictive capability of WSA–Enlil in simulating a more complicated series of CME events, based on shock-arrival time estimates and the gross features of the solar-wind parameters captured by the modeling system. We select for this study a succession of three halo CME events that occurred in August 2011. These events were initially observed by the *SOlar and Heliospheric Observatory* (SOHO) *Large Angle and Spectrometric COronagraph* (LASCO: Brueckner *et al.*, 1995) on 2 August 07:06 UT, 3 August 14:18 UT, and 4 August 04:18 UT in the C3 field of view. They were selected in part because at the time the STEREO-A and -B spacecraft viewed the CMEs as limb events so that the CME leading edges could be easily tracked. Such observations help constrain the initial CME geometries (*e.g.* angular width) during the manual cone-fitting process.

Although there are a larger number of imaging and *in-situ* observational studies that discuss successive, interacting halo CME events (*e.g.* Burlaga, Plunkett, and St. Cyr, 2002; Gopalswamy *et al.*, 2002; Farrugia *et al.*, 2006; Lugaz, Vourlidas, and Roussev, 2009; Liu *et al.*, 2012; Temmer *et al.*, 2012; Möstl *et al.*, 2012; Martinez-Oliveros *et al.*, 2012; and references therein), there are relatively fewer studies that focus on Sun-to-Earth 3D numerical simulations of these events (*e.g.* Lugaz, Manchester, and Gombosi, 2005; Lugaz *et al.*, 2008; Webb *et al.*, 2009; Shen *et al.*, 2011). Such 3D-modeling studies are valuable for providing global overviews of events and insights into the dynamics of CME–CME interactions, evolution, and propagation. One of the main goals of this article is to demonstrate the advanced WSA–Enlil cone-modeling system in simulating more complicated events such as multiple, interacting halo CMEs. A detailed analysis of the CME events using imaging and *in-situ* observations is not presented here since that is beyond the scope of this modeling study.

In Section 2, we briefly describe our approach in using the geometrical cone tool together with white-light coronagraph images at L_1 and at STEREO to obtain our ensemble of cone parameters for each of the three CME events. One objective of this study is to investigate how the exclusion or inclusion of additional CMEs in the simulations may affect the modeling results. Thus, we present in Section 3 the ensemble-modeling results in which the CME events are simulated separately from each another (*e.g.* only one CME cloud is specified in one simulation). In Section 4 we present an ensemble set of results when two CMEs are specified in a single simulation and discuss the factors that contribute to the improvements. For the preceding CME in each two-CME case presented, the best-fit ensemble member is selected and used throughout the ensemble modeling of the succeeding CME. Lastly, in Section 5 we show that the modeling results closely match the *in-situ* observations when all

three CME events are specified in a single simulation. Here, the best-fit ensemble members for the two preceding CMEs are used throughout the ensemble modeling of the third CME. In Section 6, we take the opportunity to compare results for the radial distances of the CME leading-edge fronts with those determined from the recently developed analytical harmonic mean (HM) approximation, which relates elongation-angle measurements from heliospheric imagers with CME radial distances. A brief summary and our concluding remarks are presented in Section 7.

2. Cone Modeling

The geometrical-cone software is used to parameterize the CMEs. This tool, which was developed at the National Oceans and Atmospheric Administration (NOAA) Space Weather Prediction Center (SWPC) (Millward *et al.*, 2013), is based on the mathematical approach of fitting cone shapes to CMEs (Zhao, Plunkett, and Liu, 2002; Xie, Ofman, and Lawrence, 2004) assuming the CME ejecta expands radially outward in a self-similar way (Zhao, Plunkett, and Liu, 2002). Realistic ranges of the initial angular width and leading-edge distance of the ejecta front are estimated with the tool together with the SOHO/LASCO (Brueckner *et al.*, 1995) line-of-sight white-light coronagraph observations. To determine the leading-edge distance and angular width of the CMEs more reliably, the STEREO-A and -B (Kaiser, 2005) solar-limb observations are used, since the halo CMEs are viewed nearly edge-on. From the fitting process, four parameters are determined: the source location of the cone axis (latitude, longitude), the half angular width of the CME, the time when the CME leading edge front reaches 21.5 $R_\odot$, and the radial speed at this location. Specific details about the NOAA/SWPC cone tool and the cone-fitting methodology used in this study can be found in Section 2 of Lee *et al.* (2013b).

During the time of the three CME events, the STEREO-A and -B spacecraft viewed them over the solar limb (STEREO-A was located at about 101° West of the Sun–Earth line, whereas STEREO-B was located at about 92° East of the Sun–Earth line). Thus, to better constrain the initial CME parameters during the cone-fitting process, we used science-level images from the STEREO-A and -B *Sun Earth Connection Coronal and Heliospheric Investigation* (SECCHI) COR2 coronagraph (secchi.nrl.navy.mil). Using these limb observations, for each CME we measured the angular width and the radial distance of its bright CME front in a similar manner to that described by Lee *et al.* (2013b) and Figure 3 of that study. To avoid the influence of modeling predictions made by researchers in the space-weather modeling community, online discussions and event details (*e.g.* from the SOHO CME alert emails and the Naval Research Laboratory space-weather discussion group) were ignored until after the ensemble simulations were completed for all three events. However, since our measurements were not made in real time, some knowledge of the CME arrivals *in-situ* was unavoidable and thereby influence our overall measurement process.

For each CME event, a number of independent cone fits were made to explore the sensitivity of the model-predicted CME arrival time to the realistic ranges of the angular width and the leading-edge distance. Specifically, ten fits were made for the 2 August 2011 CME (hereafter CME1), eight fits were made for the 3 August 2011 CME (hereafter CME2), and five fits were made for the 4 August 2011 CME (hereafter CME3). More fits were made for CME1 because it was harder to fit the cone ellipse over the fainter CME material than for the brighter and better defined features of CMEs2 and 3. To make each new independent fit, the LASCO images were reloaded into the NOAA/SWPC cone tool to ensure that all of the
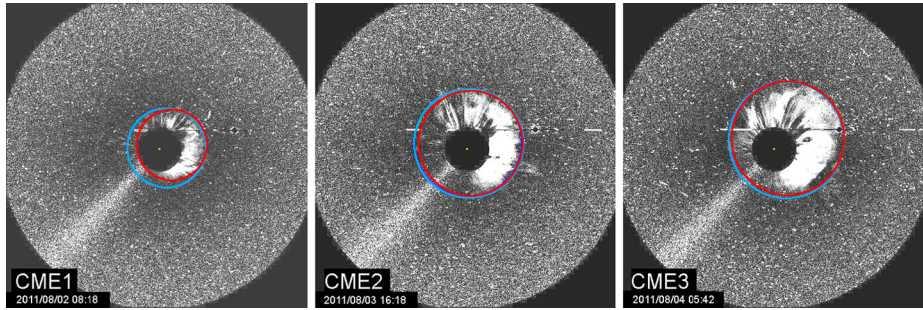
Figure 1 Example set of cone ellipses superposed on the differenced SOHO/LASCO-C3 white-light images for the CMEs on (left) 2 August, (middle) 3 August, and (right) 4 August. The red (innermost) and blue (outermost) ellipses represent the minimum to maximum range of the angular widths that were used to make the fittings for each CME shown. The range of values is listed in Table 1. The LASCO-C3 has a field of view of 3.8 $R_\odot$ to 32 $R_\odot$.

parameters were reset to the software default values. This includes the brightness and contrast settings. For each fit, slightly different values for the angular width and leading-edge distance were used, where variations were guided by the values obtained from the STEREO observations. In practice, the variations of the cone values for the angular width and leading-edge distance were obtained depending on the placement and size of the cone ellipse over the bright ejecta material in the differenced coronagraph images. Figure 1 (left to right) shows the range of cone fits superposed over the LASCO differenced images of CME1, CME2, and CME3. The blue and red ellipses illustrate the range of the angular widths that are used and the variations in the placements of the ellipses during the fitting process for each CME. Table 1 lists the range of cone parameter values used for each CME.

The CME events were simulated using the WSA–Enlil solar-corona–solar-wind model. The WSA coronal model (version 2.2.2) provides v_r and B_r at 21.5 $R_\odot$, the Enlil inner boundary. The Enlil model (version 2.6c, with the default ambient settings a3b2) simulates the solar-wind flow by calculating the solar-wind velocity, density, temperature, magnetic-field strength and polarity throughout the inner heliosphere. We used the medium-resolution spherical uniform-mesh grid consisting of $320 \times 60 \times 180$ ($r \times \theta \times \phi$) grid points. The spacings between each grid point in the radial, latitudinal, and longitudinal directions are 0.67 $R_\odot$, 2°, and 2°, respectively. In addition, the number density at the Enlil inner boundary was set to 150 cm^{-3} instead of to the default value of 200 cm^{-3}. To simulate a CME, Enlil calculates the ambient steady-state solar-wind solution and then at a prescribed time determined from the geometrical cone tool injects a pressure pulse at 21.5 $R_\odot$. To drive the background solar wind, we used the daily updated (DU) synoptic maps of the photospheric magnetic-field distribution from the National Solar Observatory (NSO) *Global Oscillation Network Group* (GONG: Harvey *et al.*, 1996).

3. Individual CME Simulations

During operational forecasting and scientific modeling of CME events, one may unknowingly simulate an individual CME event that is, in fact, part of a series of multiple halo-CME events. Thus, in this section we investigate how the exclusion and inclusion of additional CMEs in the simulations may affect the modeling results of a multi-CME event. We thus begin by simulating each of the three CME events separately, *i.e.* only one CME cloud is

Table 1 Cone-fit parameters for the CMEs of 2 to 4 August 2011. The fit numbers in each ensemble set correspond to the numbers shown in Figures 2 – 4 of our modeled results. The second and third columns contain the cone-axis latitude and longitude. The full angular width of the CME is listed in the fourth column. The fifth and sixth columns list the time and speed when the CME crosses 21.5 R$_\odot$.

Event	Fit	Source location		Full cone width [°]	Time [UT] at 21.5 R$_\odot$	V_R [km s^{-1}] at 21.5 R$_\odot$
		Lat [°]	Lon [°]			
2 August 2011	1	7	7	68	12:01	544
	2	8	7	76	12:13	583
	3	7	7	68	11:26	639
	4	8	11	66	11:16	711
	5	4	16	56	10:52	728
	6	8	11	58	10:47	729
	7	9	8	56	10:31	733
	8	9	10	60	10:49	753
	9	2	13	48	10:07	863
	10	9	9	50	09:50	961
3 August 2011	1	9	1	60	17:46	718
	2	9	2	60	17:30	824
	3	10	2	58	17:17	855
	4	9	3	56	17:07	888
	5	8	0	56	17:06	914
	6	9	2	50	16:41	955
	7	8	1	48	16:17	974
	8	9	1	50	16:30	1038
4 August 2011	1	13	9	64	06:30	1236
	2	12	10	68	06:35	1267
	3	12	9	58	06:12	1394
	4	12	8	60	06:12	1449
	5	11	6	56	05:54	1512

specified for one WSA–Enlil simulation. In doing so, it is assumed that CMEs 1, 2, and 3 do not interact with each other, nor significantly modify the background solar wind and will be observed to arrive separately at 1 AU. The number of WSA–Enlil runs generated for each event depends on the number of cone fits that were made for each CME. Figures 2, 3, and 4 show the ensemble modeling results for each event (*i.e.* the sets of color time-series seen in the figures).

To drive the background solar wind, we used the GONG DU maps for Carrington Rotation 2113, as listed in Table 2. Specifically, for the ensemble modeling of CME1 (Figure 2), CME2 (Figure 3), and CME3 (Figure 4), we used Map1, Map2, and Map3. These maps were available shortly after the occurrence of each event and were thus selected for the simulations.

Figures 2 – 4 show the *in-situ* solar-wind measurements from the *Advanced Composition Explorer* (ACE) data set (omniweb.gsfc.nasa.gov) (black time-series) together with the ensemble modeling results. In each event plot, the different color time-series corresponds to independent simulation cases whereby the cone CMEs are parameterized according to the
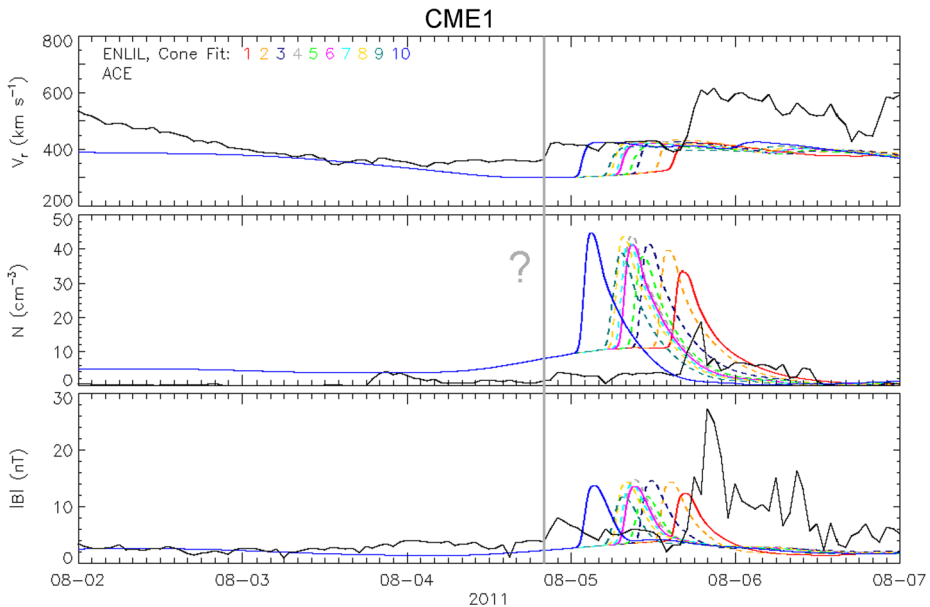
CME1

Figure 2 WSA–Enlil simulation results for the CME1 (2 August 2011) radial solar-wind speed, density, and total magnetic field at 1 AU. The modeling ensemble (colored lines) is overplotted with the one-hour-resolution Level-2 ACE observations (solid-black line). The solid color lines (left to right) are used to distinguish the earliest, average, and latest arrival-time predictions. The gray-vertical line marks the increase in the solar-wind speed at $\approx 20{:}00$ UT 4 August. For our discussion in Section 3, we assume that this speed increase indicates the approximate (observed) shock-arrival time of CME1 at Earth. The cone-fit numbers in the velocity panels correspond to the numbers listed in Table 1. Map1 (see Table 2) is used to simulate the background solar wind.

cone-fit values listed in Table 1. The radial solar-wind speed, density, and the total magnetic field are shown in the top, middle, and bottom panels, respectively.

The top panels in Figures 2 – 4 show three distinct step-wise increases in the observed solar-wind speed (black lines), commencing around 20:00 UT 4 August, 17:00 UT 5 August, and 21:00 UT 6 August, as indicated by the gray-vertical line shown in each figure. For the following discussion, we assume that the increased speeds are caused by the separate arrivals of shock fronts of CME1, CME2, and CME3, respectively. Referring to Figure 2 (top panel), the peak solar-wind speeds of the modeling ensemble for CME1 (colored lines) are similar to the values observed (black line) starting after 20:00 UT 4 August (vertical-gray line). However, the modeled pre-CME background solar-wind speeds are lower than the observed values by about $50 - 100 \ \mathrm{km \, s^{-1}}$, which explains the delay in the modeled CME1 arrival times. Specifically, the ensemble lags behind the observed arrival time by about 11 hours based on the average ensemble member fit number 6 (second solid line, shown in magenta). If we refer to our earliest and latest prediction in our ensemble (leftmost and rightmost solid lines, shown in blue and red, respectively) the spread from our average prediction is approximately $+6/-7$ hours. When examining the modeled densities, Figure 2 (middle panel) shows that the modeled pre-CME background solar-wind densities are much higher than the observed values, which are very low, about less than 2 cm^{-3} for several days before the CME arrival. Upon the arrival of CME1, there is a modest increase in the observed densities (at the beginning of 20:00 UT, as marked by the vertical-gray line), whereas the ensemble of modeled density values are dramatically higher. The modeled values for the
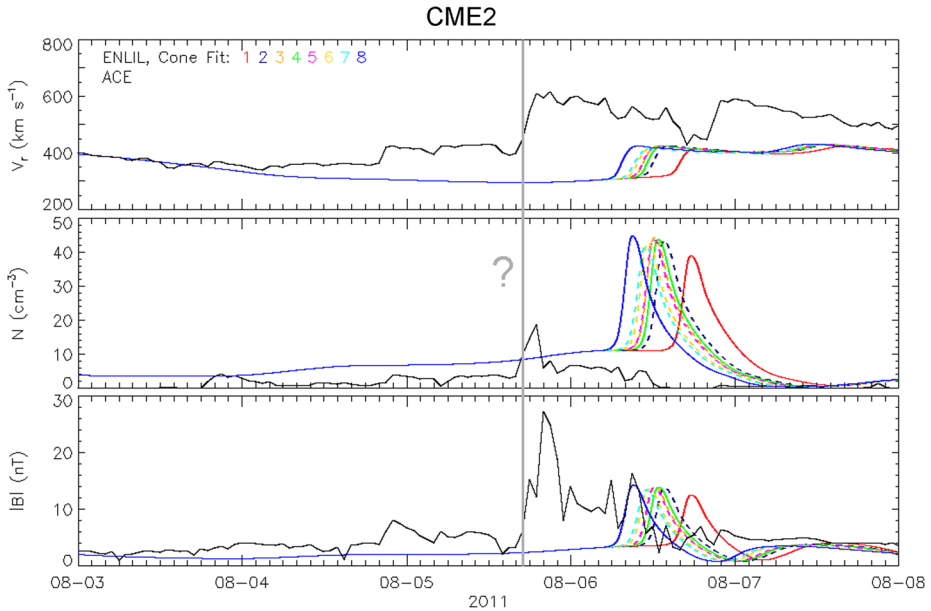
Figure 3 WSA–Enlil simulation results for the CME2 (3 August 2011) radial solar-wind speed, density, and total magnetic field at 1 AU. The modeling ensemble (colored lines) is overplotted with the one-hour-resolution Level-2 ACE observations (solid-black line). The solid color lines (left to right) are used to distinguish the earliest, average, and latest arrival-time predictions. The gray-vertical line marks the increase in the solar-wind speed at ≈ 17:00 UT 5 August. For our discussion in Section 3, we assume that this speed increase indicates the approximate (observed) shock-arrival time of CME2 at Earth. The cone-fit numbers in the velocity panels correspond to the numbers listed in Table 1. Map2 (see Table 2) is used to simulate the background solar wind.

magnitude of the magnetic field (Figure 2, bottom panel) are also higher, about twice the observed values for CME1.

Figure 3 shows a comparison of the modeling results for CME2 compared with the observations. Between 16:00 UT 5 August and 16:00 UT 6 August, the observations show increases in the solar-wind speed (top panel), density, (middle panel), and magnetic field (bottom panel). If we assume that the increased values are caused solely by the arrival of CME2, then the average modeled shock-arrival time, based on fit number 4 (second solid line, shown in green) lags behind the observed arrival by about 18 hours with a spread of four–five hours from the average prediction. In addition, Figure 3 (top panel) shows that the peak amplitudes of the modeled CME speeds (top panel) and magnetic field (bottom panel) are much lower than those that are observed between 16:00 UT 5 August and 20:00 UT 6 August. In contrast, the modeled densities for CME2 (middle panel) are significantly higher than the observations. As for CME1, here the modeled pre-CME background solar-wind densities are also much higher than the observed values.

If we assume in Figure 4 that the increase in the solar-wind speed observed at ≈ 21:00 UT 6 August (vertical gray line) is caused by CME3, then the ensemble of modeled arrival times is ahead of the observed arrival time by about 22 hours based on the average ensemble member 3 (second solid line, shown in green). Here, the spread around this average prediction is two hours. However, there are no increases in the observed density and magnetic-field values (middle and bottom panel) around 21:00 UT 6 August that would indicate the arrival of CME3. Instead, as we show in the next section, it is likely that CME3 merged with CME2 as
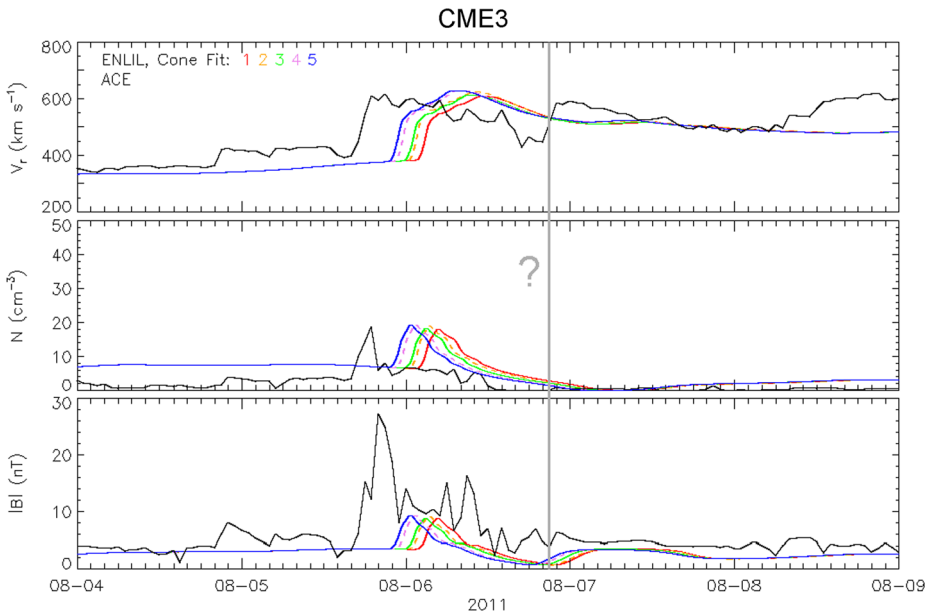
Figure 4 WSA–Enlil simulation results for the CME3 (4 August 2011) radial solar-wind speed, density, and total magnetic field at 1 AU. The modeling ensemble (colored lines) is overplotted with the one-hour-resolution Level-2 ACE observations (solid-black line). The solid color lines (left to right) are used to distinguish the earliest, average, and latest arrival-time predictions. The gray-vertical line marks the increase in the solar-wind speed at $\approx$ 21:00 UT 6 August. For our discussion in Section 3, we assume that this speed increase indicates the approximate (observed) shock-arrival time of CME3 at Earth. The cone-fit numbers in the velocity panels correspond to the numbers listed in Table 1. Map3 (see Table 2) is used to simulate the background solar wind.

Table 2 GONG daily updated (DU) maps for Carrington Rotation 2113.

DU map leading-edge longitude [°]	Last magnetogram date [UT]	Shorthand name
250	02 August 2011/23:14	Map1
239	03 August 2011/20:04	Map2
225	04 August 2011/21:14	Map3

they propagated toward Earth. Similar to CMEs 1 and 2, the modeled pre-CME background solar-wind densities are much higher than the observed values.

4. Simulating Two CMEs Together

4.1. CME1 and CME2

The modeling results begin to resemble the observations more when two CMEs are specified in a simulation. Figure 5 shows the modeling results for CME1 and CME2. Here, the fixed ensemble cone member number 10 is used exclusively for CME1 (leftmost solid line, shown in blue in Figure 2), and thus the spread in the modeled arrival times as seen in Figure 5 is due
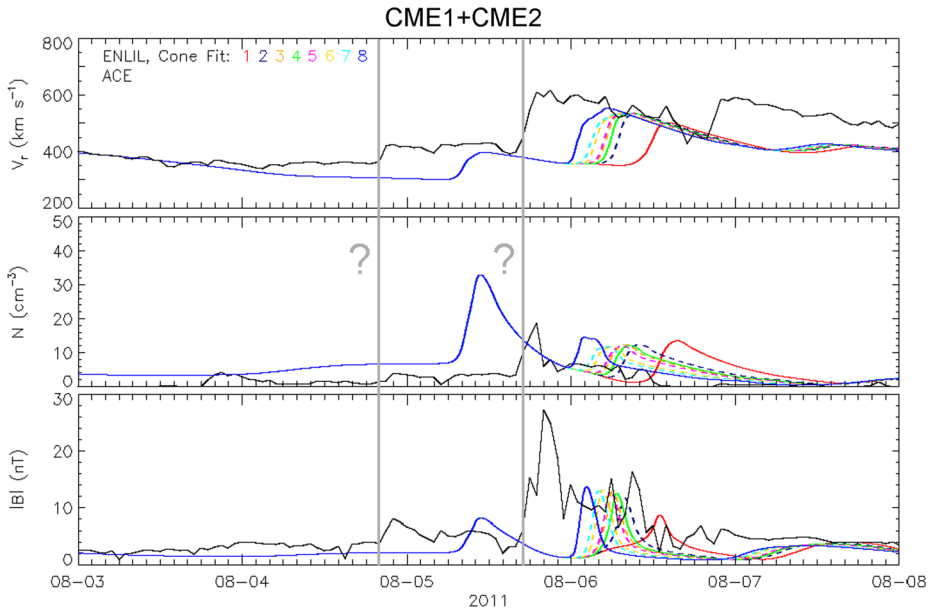
Figure 5 WSA–Enlil simulation results for the CME1+CME2 radial solar-wind speed, density, and total magnetic field at 1 AU. The modeling ensemble (colored lines) is overplotted with the one-hour-resolution Level-2 ACE observations (solid-black line). The solid color lines (left to right) are used to distinguish the earliest, average, and latest arrival-time predictions. The gray-vertical lines mark the increase in the solar-wind speeds at ≈ 20:00 UT 4 August and ≈ 17:00 UT 5 August. For our discussion in Section 4.1, we assume that these increased speeds indicate the approximate (observed) shock-arrival times of CME1 and CME2 at Earth. The ensemble cone member number 10, as listed in Table 1, is used for CME1 such that the ensemble spread shown (colored lines) is due to the variations in the cone parameters for CME2. Map2 (see Table 2) is used to simulate the background solar wind.

to cone-parameter variations for CME2. Fit number 10 was selected for CME1 because the use of this cone-parameter set produced the earliest arrival time in the modeling ensemble (see Figure 2). To simulate the background solar wind, we used Map2 since this provides a more updated background solar-wind description than the older Map1. (We recall that Map1 was used to simulate CME1 and Map2 to simulate CME2.)

When CME1 and CME2 are simulated together, the two-step increase in the solar-wind values is reproduced by the model (colored lines in Figure 5, top panel). The increases in the modeled solar-wind speed occur at 08:00 UT on 5 August for CME1 and at 06:00 UT on 6 August for the average ensemble member of CME2 (fit 4, green) such that the modeled two-step structure lags the observed structure by about 13 hours. Based on the average ensemble member for CME2, when CME1 is simulated before CME2, the modeled arrival times improve by about five hours for CME2. On the other hand, the spread in the modeling ensemble increases by about one hour such that the spread around the average prediction is now five hours. The modeled peak solar-wind speed values for CME2 are higher and more comparable to the observed speeds. The modeled peak-density values for CME2 (shown in Figure 5, middle panel, between 6 August and 7 August) are noticeably lower and more comparable to the observed values. Regardless of the inclusion of CME1, the peak values for the CME2 magnetic-field signature (bottom panel) remains unchanged when compared with the results derived from its individual simulation (Figure 3, bottom panel).
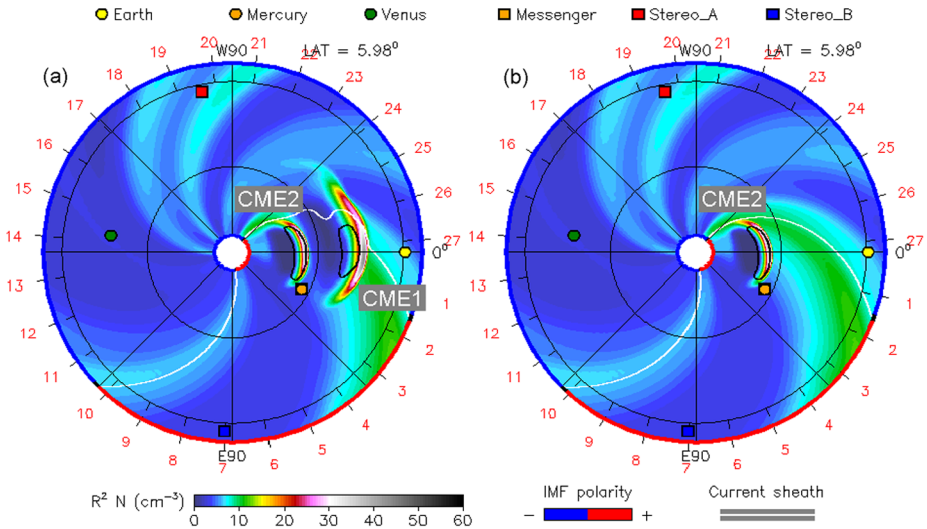
Figure 6 Ecliptic view at 02:00 UT 5 August 2011 of the solar-wind densities for (a) CME1+CME2 and (b) CME2. The black contour lines are based on the velocity contours of the CMEs (see Figure 13). Fits number 10 and 8 are used for CME1 and CME2 (see Table 1). Map2 is used to simulate the background solar wind (see Table 2).

By simulating CME2 together with CME1, the modeling results improve because the background solar wind due to CME1 and propagating ahead of CME2 is relatively more accurate. Figure 6a shows that as CME1 propagates toward Earth, a more rarefied solar-wind environment (dark-blue region) is created behind it. Rather than propagating into a denser solar-wind stream (Figure 6b, green), CME2 propagates into a more rarefied solar-wind environment that is created by the earlier passage of CME1 (Figure 6a, dark-blue region). Thus, the CME2 cloud is less compressed (compare Figure 7a with Figure 7b), propagates faster, and arrives at Earth sooner. From the global simulation results, CME2 does not merge with CME1 as they travel toward Earth. Thus, the differences in the modeled CME2 results at 1 AU (compare Figures 3 and 5) are directly related to the different background solar-wind conditions into which CME2 propagates.

The modeled results for CME1 do not improve when it is simulated together with CME2. Specifically, the modeled arrival time is more delayed (from 6 to 12 hours) and the solar-wind speeds are lower than the observed values. On the other hand, there is a slight improvement in the modeled solar-wind densities and magnitude of the magnetic-field values, in which the modeled values for CME1 both decrease. However, the modeled background densities during the time leading up to the arrival of CME1 are still too high. Overall, the changes in the modeled values for CME1 are due to the use of a different input map into WSA–Enlil to simulate the background solar-wind conditions. Whereas Map1 was used to simulate CME1 on its own (Figure 2), here the more recent Map2 was used. Given that Map1 is about one day older than Map2, the global photospheric magnetic fields are different enough to produce a different set of background solar-wind conditions in the WSA–Enlil simulations. It should be noted that for future simulations of CME events, the Air Force Data Assimilative Photospheric flux Transport (ADAPT) model (Arge *et al.*, 2010, 2011; Henney *et al.*, 2012) will provide updates of the photospheric magnetic-field distribution to WSA, which will then provide continuously updated boundary conditions to Enlil.
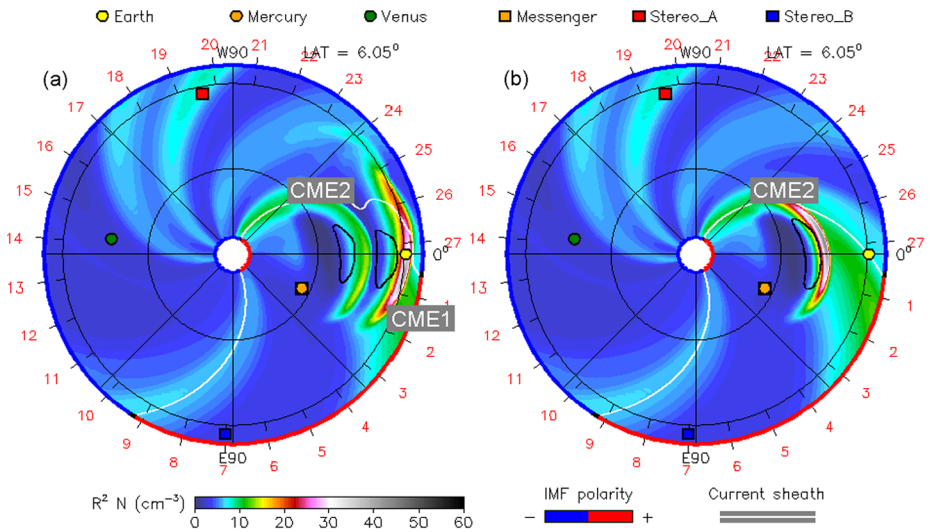
Figure 7 Ecliptic view at 08:00 UT 6 August 2011 of the solar-wind densities for (a) CME1+CME2 and (b) CME2. The black contour lines are based on the velocity contours of the CMEs (see Figure 13). Fits number 10 and 8 are used for CME1 and CME2 (see Table 1). Map2 is used to simulate the background solar wind (see Table 2).

4.2. CME2 and CME3

The modeled arrival time further improves when CME2 is simulated together with CME3 (Figure 8). To simulate the background solar wind, we used Map3 since this provides a more updated representation of the photospheric magnetic fields during the time of the 4 August 2011 CME event. Here, the fixed ensemble cone member 8 is used for CME2 such that the spread in the modeling ensemble as shown is due to the cone-parameter variations for CME3. Fit number 8 is selected for CME2 because the use of this cone-parameter set produced the earliest arrival time in the modeling ensemble (see Figure 3).

The top panel of Figure 8 shows an increase in the modeled solar-wind speeds around 19:00 UT 5 August followed by a secondary increase around 08:00 UT 6 August, indicating the arrivals of CME2 and CME3. By modeling CME2 with CME3, the arrival of the second step-wise increase in the solar-wind speed is better captured than by simulating CME2 or CME3 on its own. Although the modeled arrival time of the third step-wise increase in the solar-wind speed appears too early (around 08:00 UT 6 August instead of 21:00 UT 6 August), this speed increase is not likely to be caused by the arrival of CME3. (We recall that in Section 3 we assumed that each of the three step-wise increases in the solar-wind speeds is due to the arrivals of CMEs 1, 2, and 3.) Instead, the lack of increased activity in the observed densities and magnetic-field values from 20:00 UT 6 August onward suggests that the observed solar-wind speeds following the third speed increase are the return of the undisturbed solar wind (for example, see the dark-blue region that follows the CME3 structure in Figure 9d, bottom panel), which the model captures very well.

Referring to the observations, the enhanced values for all three solar-wind parameters shown between 16:00 UT 5 August to 20:00 UT 6 August are most likely caused by the arrival of the merged structures of CME2 and CME3. From the global ecliptic solutions, Figures 9b and 9c (bottom panels) show that just beyond 0.5 AU, CME3 catches up and
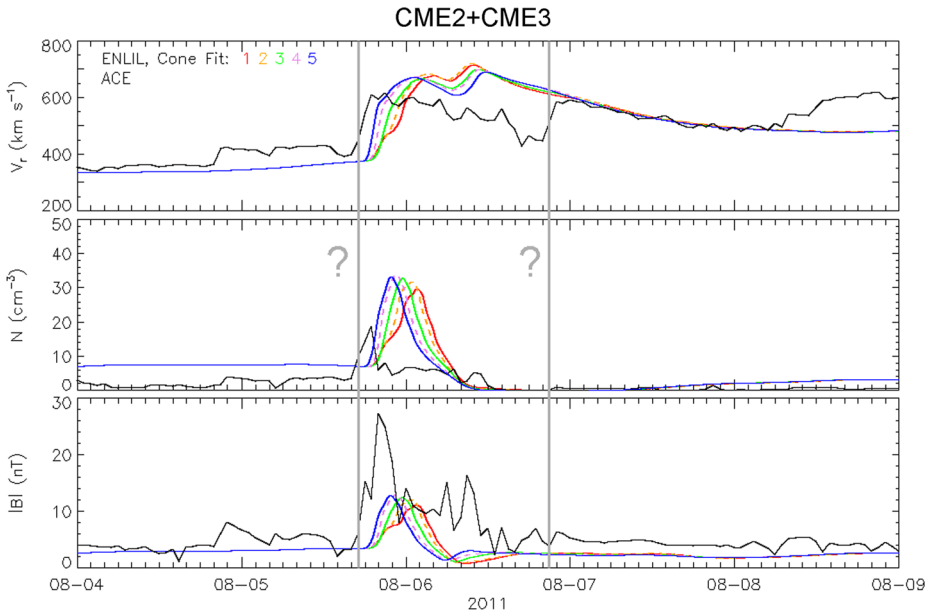
Figure 8 WSA–Enlil simulation results for the CME2+CME3 radial solar-wind speed, density, and total magnetic field at 1 AU. The modeling ensemble (colored lines) is overplotted with the one-hour-resolution Level-2 ACE observations (solid-black line). The solid color lines (left to right) are used to distinguish the earliest, average, and latest arrival-time predictions. The gray-vertical lines mark the increase in the solar-wind speeds at $\approx 17:00$ UT 5 August and $\approx 21:00$ UT 6 August. For our discussion in Section 4.2, we assume that these increased speeds indicate the approximate (observed) shock-arrival times of CME2 and CME3 at Earth. The ensemble cone member number 8, as listed in Table 1, is used for CME2 such that the ensemble spread shown (colored lines) is due to the variations in the cone parameters for CME3. Map3 (see Table 2) is used to simulate the background solar wind.

interacts with CME2. At 1 AU, CME2 and CME3 arrive as a merged CME structure (Figure 9d, bottom panel). Because the merged structure propagates into a dense solar-wind stream (appearing in cyan throughout Figure 9, bottom panels), the leading edge of the merged structure becomes more compressed and a large, single, sharp rise in the modeled densities is produced, as shown in Figure 8 (middle panel). In addition to the compression of the leading edge, the modeled densities for the merged CME structure are also very high because of the higher modeled pre-event background values (see Figure 8, middle panel). For the magnetic-field values (Figure 8, bottom panel), the model also produces a single increase in the values, although they are underestimated compared with the observed values. Based on the average ensemble member for CME3 (fit 3, green line in Figure 8), the modeled shock-arrival time of the merged CME structure lags behind the observed time by about three hours, with a spread of two–three hours around the average prediction. Note that the model misses the first step-wise increase in the solar-wind speed (top panel); this is presumably the arrival of CME1, which is not included in this simulation.

4.3. CME1 and CME2 with Map3

In the previous section, the use of Map3 yielded better modeling results, particularly in the background solar-wind speeds during the two days before the arrival of the merged CME2+CME3 structure. As a result, the ensemble of arrival times for the merged CME
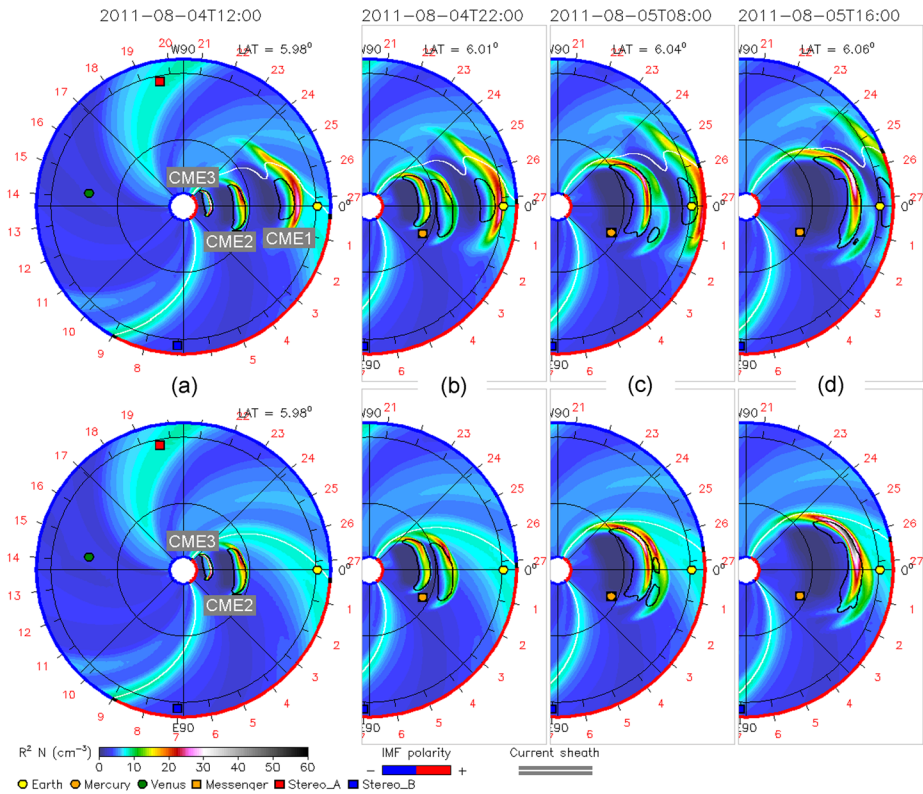
Figure 9 Ecliptic view of the evolution of (top row) CME1+CME2+CME2 and (bottom row) CME2+ CME3. The colors shown are for the solar-wind density. (top row) Fits number 10, 8, and 1 are used for CME1, CME2, and CME3 (see Table 1 for details). (bottom row) Fits number 8 and 1 are used for CME2 and CME3. For both cases, Map3 is used to drive the background solar wind (see Table 2). Earth is shown on the right of each panel as a filled yellow circle.

structure better matched the observed arrival time. As part of our ensemble modeling, it is useful to simulate the CME1+CME2 events using Map3 as input and contrast these results with those that are shown in Figure 5 in Section 4.1 when the older Map2 was used.

Figure 10 shows that the modeled solar-wind speeds (top panel) for CME1 and CME2 match the observations better when Map3 is used to generate the background solar wind. In particular, the modeled background solar-wind speeds starting on 00:00 UT 3 August nearly overlap with the observed values. With a more accurately modeled background solar wind, the modeled arrival time and the speed values for CME1 now overlap with the first step-wise increase observed at 20:00 UT 4 August (vertical-gray line). For CME2, the ensemble of solar-wind speeds better overlap with the second step-wise speed increase observed around 17:00 UT 5 August. Although the modeled densities are still too high, as seen for the background values during the days before the CME arrival and for CME1, overall the peak values are lower than when Map2 was used (Figure 5, middle panel). For CME2, the ensemble of density values are also slightly lower, but the values better overlap the observed values than those that were shown previously in Figure 5 (middle panel). For the magnetic-field results (Figure 10, bottom panel), the modeled results show an improvement in the overall arrival time.
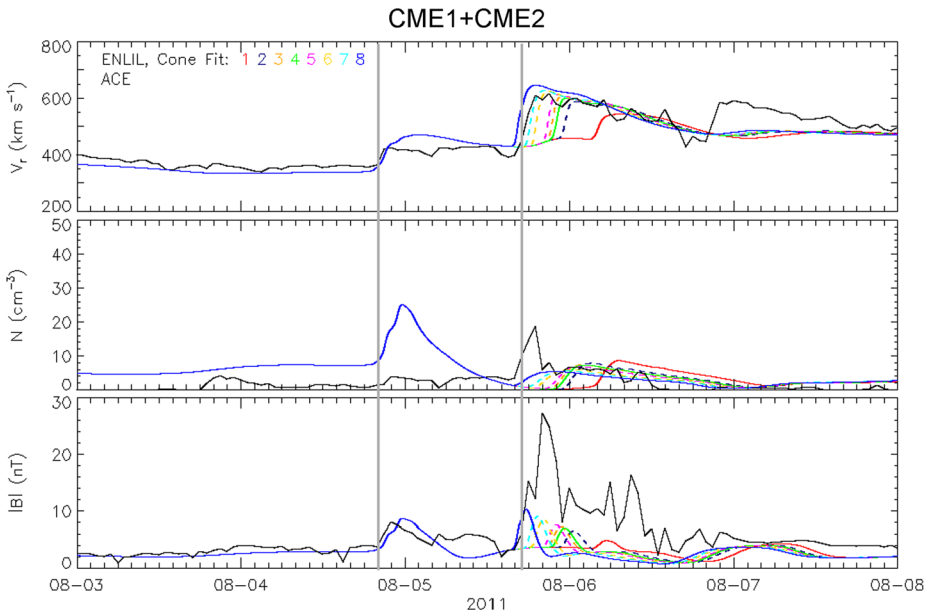
Figure 10 WSA–Enlil simulation results for the CME1+CME2 radial solar-wind speed, density, and total magnetic field at 1 AU. Map3 is used for simulating the background solar wind in comparison to Map 2 used in Figure 5. The modeling ensemble (colored lines) are overplotted with the one-hour resolution Level-2 ACE observations (solid-black line). The solid color lines (left to right) are used to distinguish the earliest, "average", and latest arrival-time predictions. The gray-vertical lines mark the increase in the solar-wind speeds at $\approx$20:00 UT 4 August and $\approx$17:00 UT 5 August. The ensemble cone member number 10, as listed in Table 1 is used for CME1 such that the ensemble spread shown (colored lines) is due to the variations in the cone parameters for CME2.

Interestingly, both the current CME1+CME2 results and the CME2+CME3 results presented in the previous section capture the general features of the observations very well, particularly those of the observed solar-wind speeds. Comparing Figure 10 with Figure 8 from the previous section, it might be argued that the speed profiles are better captured when CME1 and CME2 are simulated together rather than CME2 with CME3. However, the CME1+CME2 modeling results miss the third step-wise increase in the solar-wind speed (beginning around 21:00 UT 6 August), whereas the modeling results for CME2+CME3 do capture this trailing background solar-wind region from 22:00 UT 6 August onward.

5. Simulating Three CMEs Together

Figure 11 shows that if all three CMEs are modeled together in a single simulation, the general features of the solar-wind observations are best captured by the model compared with the two-CME cases that were discussed in the previous section. Here, the ensemble members 10 and 8 are used for CME1 and CME2 such that the spread in the arrival-time ensemble shown are due to the cone-parameter variations of CME3. To simulate the background solar wind, Map3 was used.

The top panel in Figure 11 shows the modeled values for the background solar-wind speeds overlapping with the observed values. Given a more accurately modeled solar-wind
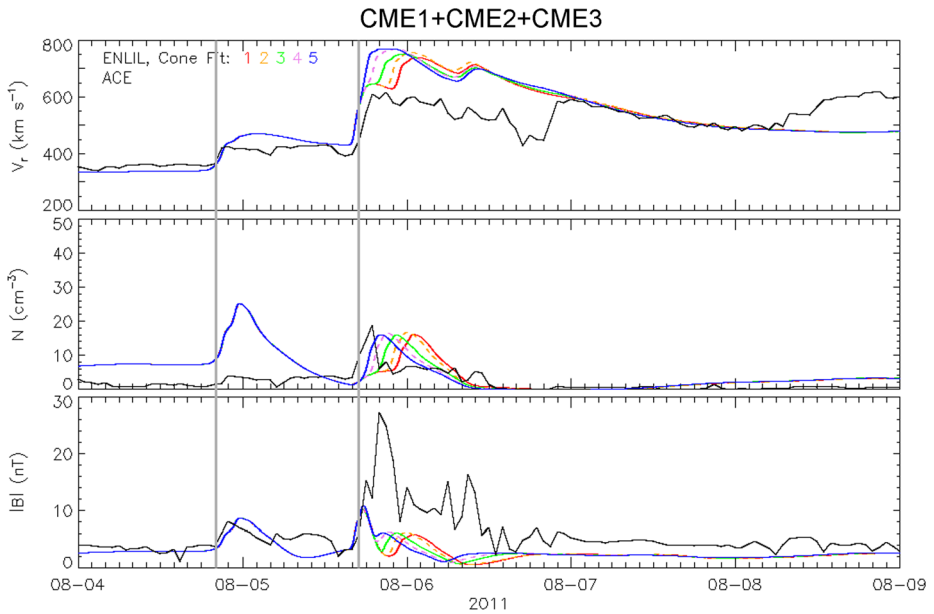
Figure 11 WSA–Enlil simulation results for the CME1+CME2+CME3 radial solar-wind speed, density, and total magnetic field at 1 AU. The modeling ensemble (colored lines) is overplotted with the one-hour-resolution Level-2 ACE observations (solid-black line). The solid color lines (left to right) are used to distinguish the earliest, average, and latest arrival-time predictions. The gray-vertical lines mark the increase in the solar-wind speeds at $\approx$ 20:00 UT 4 August and $\approx$ 17:00 UT 5 August. These increased speeds indicate the approximate (observed) shock-arrival times of CME1 and the merged CME2+CME3 structure at Earth. The ensemble cone members number 10 and number 8 are used for CME1 and CME2, such that the ensemble spread shown (colored lines) is due to the variations in the cone parameters for CME3. Map3 (see Table 2) is used to simulate the background solar wind.

background, the modeled speeds for the first step-wise increase (CME1) match the observations very well in terms of the arrival time (first gray-vertical line) and the peak-speed values. Subsequently, the observed arrival time of the second step-wise increase for the merged CME2+CME3 structure (commencing at 17:00 UT 4 August, second gray-vertical line) is also captured very well by the modeling ensemble. Although the peak-speed values here are much higher than the observations, the ensemble of arrival times nearly overlaps the observed value. For the solar-wind speeds that trail the multi-CME activity, the modeled values overlap the observed speeds even though the model misses the third step-wise increase in the speed that occurs at 21:00 UT 6 August.

The arrival times of the CME1 densities and magnetic fields (Figure 11, middle and bottom panels) match the observed values well. However, in contrast to the amplitude of the peak magnetic-field values, the peak densities are too high, which is in part due to the high modeled background values that are seen before the CME1 arrival. (Referring to Figures 9a–9c, top panels, CME1 propagates into and is compressed by the preceding dense solar-wind stream, shown in cyan). For the merged CME2+CME3 structure, the peak densities and magnetic-field values better match the observed values (Figure 11, middle and bottom panels) than for the two-CME case shown in Figure 8. The improvement of the modeled densities for the merged CME2+CME3 in the three-CME case is due to the CME1 cloud that is propagating ahead. Figures 9a–9d (top panels) show that as CME1 propagates
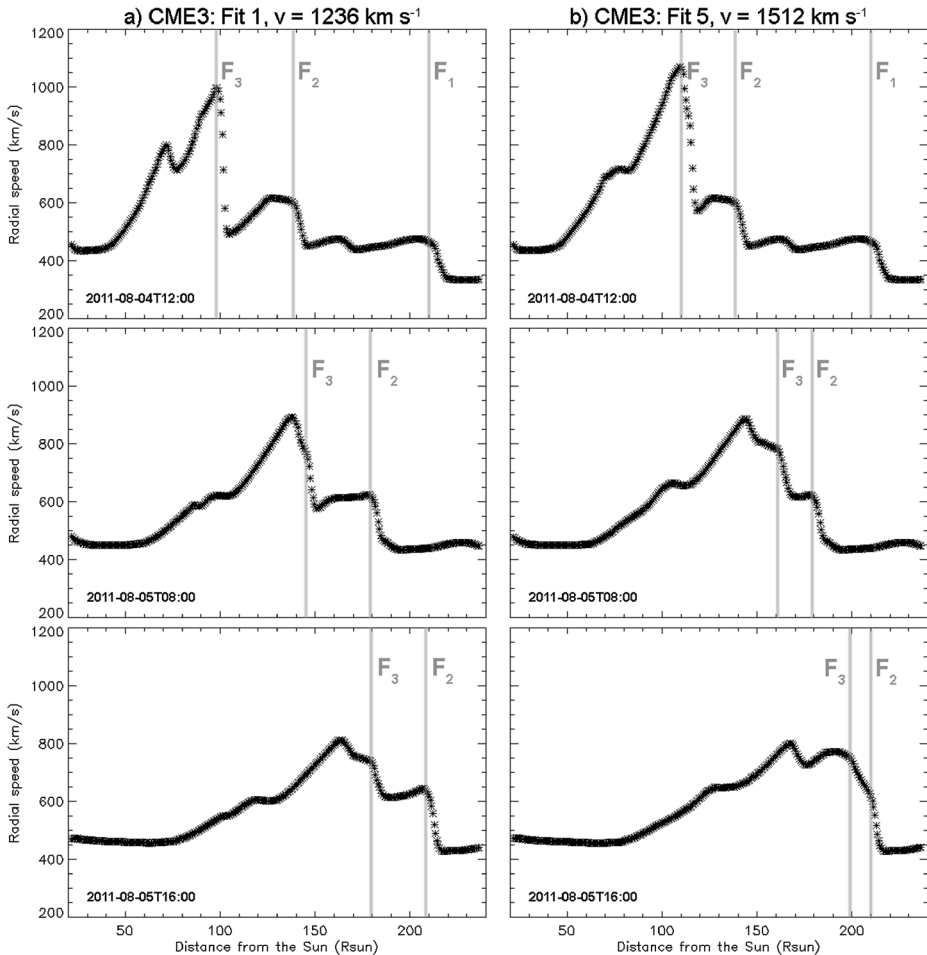
Figure 12 The CME speed profiles along the Sun–Earth line, in the Ecliptic plane, are shown for three time steps. Earth is located at about 215 $R_\odot$. The cone members used for CME1 and CME2 are fits number 10 and 8, whereas the cone members used for CME3 are fits number 1 (column a) and 5 (column b). The leading-edge fronts for CMEs 1, 2, and 3 are marked by gray-vertical lines and are labeled F1, 2, and 3, respectively.

toward Earth, a rarefaction region forms behind it and in front of the merged CME2+CME3 structure. Thus, the merged CME structure is less compressed (compare the top and bottom panels of Figures 9c and 9d) and a lower set of values is observed for the peak densities in Figure 11 (middle panel).

We examined the ensemble of modeled arrival times for the merged CME2+CME3 structure in Figure 11 (top panel) in more detail and found that even though there is an ensemble spread of about six hours, the initial arrival time for each ensemble member occurs at the same time (around 17:00 UT 4 August). The fastest ensemble member for CME3 (leftmost solid line, shown in blue) might be expected to have an earlier arrival time than the slowest ensemble member (rightmost solid line, shown in red). To gain a better understanding, it is useful to plot the speed profiles of the three CMEs along the Sun–Earth line in the Ecliptic
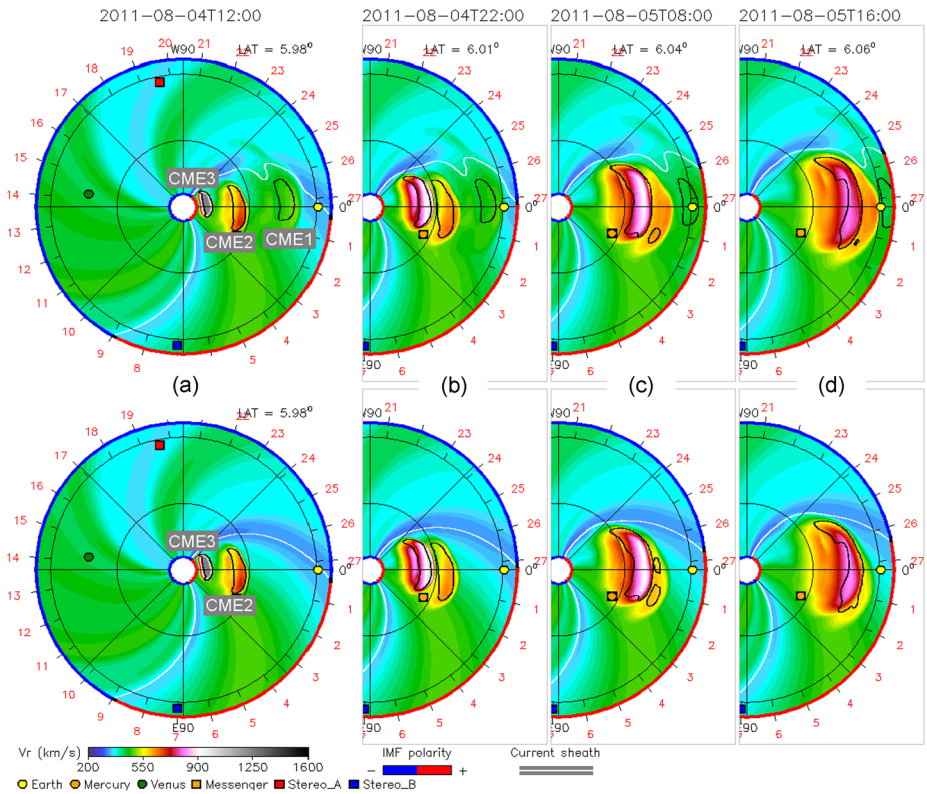
Figure 13 Ecliptic view of the evolution of (top row) CME1+CME2+CME2 and (bottom row) CME2+ CME3. The colors shown are for the solar-wind radial speed. (top row) Fits number 10, 8, and 1 are used for CME1, CME2, and CME3 (see Table 1 for details). (bottom row) Fits number 8 and 1 are used for CME2 and CME3. For both cases, Map3 is used to drive the background solar wind (see Table 2). Earth is shown on the right of each panel as a filled-yellow circle.

plane. Figure 12 shows the radial speed profiles for CMEs 1, 2, and 3, where the high-speed fronts are marked with gray-vertical lines and labeled F1, F2, and F3. The slowest CME3 ensemble member (fit 1 in Figure 11) is used throughout Figure 12a, whereas the fastest CME3 ensemble member (fit 5 in Figure 11) is used throughout Figure 12b. The ensemble cone members used for CME1 and CME2 are the same as those that were used for the results shown in Figure 11.

When simulating the slowest CME3 ensemble member with CME1+CME2, Figure 12a shows the CME2 high-speed front reaching Earth (at about 215 $R_\odot$) before the CME3 high-speed front catches up with it. The global Ecliptic solutions in Figures 13b – 13d (top panels) shows this as well, where the CME3 leading edge front catches up and interacts with the trailing part of CME2 but never catches up to the CME2 leading-edge front before the structure reaches Earth (filled-yellow circle on the right side of each panel). In Figure 11 (rightmost solid line, shown in red) it is apparent that the initial arrival time commencing around 17:00 UT 5 August is caused by the arrival of CME2, and that the secondary increase in the modeled speed commencing at 22:00 UT 5 August is due to the arrival of CME3.

For the fastest CME3 ensemble member, Figure 12b (top and middle panels) shows that CME3 catches up to CME2 faster than in the previous case. By the time that CME2 reaches Earth (bottom panel), the leading-edge front of CME3 nearly overlaps the leading-edge front of CME2. Thus, when the structure arrives at 1 AU, a single increase in the solar-wind speed is observed for the merged CME2+CME3 structure, and the initial arrival commences at a similar time as for the slowest ensemble member case.

5.1. Comparison with the CME1+CME2 Case

Comparing only the blue time series from the CME2+CME3 case (Figures 10) and the CME1+CME2+CME3 case (Figure 11), it can be argued that the two-CME case produces better results, particularly for the solar-wind speeds. However, we argue that the three-CME case produces the best overall results in comparison. (We recall that for both cases, the same input map, Map3, and ensemble members were used for CME1 and CME2, *e.g.* fits 10 and 8.)

In the two-CME case, the modeled solar-wind speeds nearly overlap the observed values for the preceding background solar wind (from 00:00 August 3 to 18:00 UT August 6) and the first two step-wise increases in the solar-wind speeds. However, the model misses the trailing solar-wind structure that commences after 20:00 UT August 6. By including CME3 in the simulation with CME1 and CME2, the trailing portion of the solar wind is captured. The model misses the steep increase in speed observed around 20:00 UT August 6 and also overestimates the modeled speeds for the second solar-wind structure observed (from 18:00 UT August 5 to 18:00 UT August 6) by about 200 km s^{-1}. Despite this overestimation, the modeled arrival time of this structure shown in the three-CME case is similar to the arrival time shown in the two-CME case. The reason for the similar arrival time, as opposed to an earlier arrival time for the three-CME case, is that CME3 does not fully overtake CME2 until after 1 AU. Instead, the leading edge of CME3 merges with the trailing portion of CME2 and nearly overlaps the leading-edge front of CME2 as they approach 1 AU (see for example Figure 12b and the related discussion).

The peak values for the density structure observed between 16:00 UT August 5 to 12:00 UT August 6 are better matched when CME3 is simulated together with CME1 and CME2. The interaction of CME3 with CME2 produces higher and steeper densities as well as an earlier arrival time. The simulation of CME3 with CME1 and CME2 does make some difference in the modeled magnetic-field values, but the detailed structures seen in the CME interaction region between 16:00 UT August 5 to 00:00 UT August 7 are mostly missing from the modeling results. This is expected since there is a lack of magnetic-cloud and flux-rope information in the CMEs. As such, there is no reason to expect the simulation details pertaining to the dynamical interaction between CME2 and CME3 to be correct.

From examining the entire ensemble of results shown in Figure 11, we capture all of the major features that are not related to the CME–CME interaction region by simulating the three CMEs together. We have demonstrated that when Map3 is used in the simulation for CME1+CME2, we are able to reproduce the preceding background solar-wind speeds as well as the background solar-wind magnitude of the magnetic field. When CME3 is included in the simulation, the solar-wind speeds trailing the interaction region are also clearly captured by the model. Although the interaction of CME3 with CME2 in the simulations produces higher solar-wind speeds for the merged CME structure, the ensemble spread in the arrival times is smaller for the solar-wind parameters shown, and the peak densities better match the observed values.

6. Comparison of Radial Distances with Heliospheric Imager Observations

Taking advantage of the fact that this is a retrospective study of the August 2011 CME events, we are able to fine-tune our selection of the different sets of input DU maps and our use of different cone parameters and their combinations for CMEs1, 2, and 3. Thus, our results presented for CME1+CME2+CME3 are based on our best-fit selections of these input factors. In part to justify our selections, we compared the CME radial distances that are calculated using the WSA–Enlil cone with those independently derived from the recently developed analytical harmonic mean (HM) approximation (Lugaz, Vourlidas, and Roussev, 2009). The HM method relates the elongation-angle measurements to the radial distances of CMEs. The elongation angles for the August 2011 CMEs were measured from time–elongation maps (J-maps: Davies *et al.*, 2009) based on observations provided by the STEREO-A/SECCHI *Heliospheric Imager*-1 and -2 (HI-1 and H1-2: Howard *et al.*, 2002). The underlying assumptions in the HM methodology are that the observed CME density structure can be modeled as a sphere whose center propagates radially outward and the heliospheric imager observes the tangent of the dense, circular CME front. Further details about the HM methodology have been given by Lugaz, Vourlidas, and Roussev (2009), in particular Sections 3 and 4, and the references therein.

Figure 14 shows the radial distance of each CME along the Sun–Earth line derived from the HM method (filled symbols) and from the WSA–Enlil cone (open symbols). With the HM method, the points of maximum brightness shown in the time–elongation maps are used to determine the CME positions. Specifically, the leading-edge distance of each CME was calculated using a fixed CME direction following Lugaz, Roussev, and Vourlidas (2009), and the distance along the Sun–Earth line was calculated using a similar methodology described by Möstl and Davies (2013). The positions out to 80 $R_\odot$ were obtained from HI-1 observations. Beyond this distance, the CME tracks for this set of events become too faint to observe, and the observations from HI-2 were used instead. Beyond 120 $R_\odot$ the CMEs become too faint even in the HI-2 observations to accurately determine the position of the CME leading edge. For the WSA–Enlil-cone results, the position of the highest density is determined by eye for each CME at each time step. To be consistent with the results shown thus far (*e.g.* Figure 11 and the top panels of Figures 9 and 13), the simulation results that used ensemble members 10, 8, and 1 for CME1, CME2, and CME3 are the values shown in Figure 14.

Within 100 $R_\odot$, the CME radial distances derived from both modeling techniques are fairly comparable for CME1 (black circles), CME2 (red triangles), and CME3 (green squares). For CME1 and CME2, the results from both methods overlap one another and show that the CMEs gradually decelerate, although a qualitative examination shows that the deceleration is slightly faster when the HM method is used. The results for CME3 from both methods also overlap for the radial distances between 20 $R_\odot$ to 100 $R_\odot$, although a stronger deceleration is shown for the HM-derived results compared to a near-constant speed from the WSA–Enlil cone. Beyond 100 $R_\odot$ the few available HM data points are unreliable (Lugaz, Vourlidas, and Roussev, 2009) for comparison. Although the HM results do not extend beyond 120 $R_\odot$, the trajectories of CME2 and CME3 imply that the two CMEs will eventually merge. Note that for all three CMEs, a transition in the number of HM data points can be seen starting at around 80 $R_\odot$. This is due to the switch of using observations from HI-1 to HI-2, the latter of which have a longer temporal cadence between new observations.

Note that at 100 $R_\odot$ the WSA–Enlil-cone results show an apparent sudden acceleration of CME3 followed by a more constant motion after 120 $R_\odot$. This acceleration is unphysical
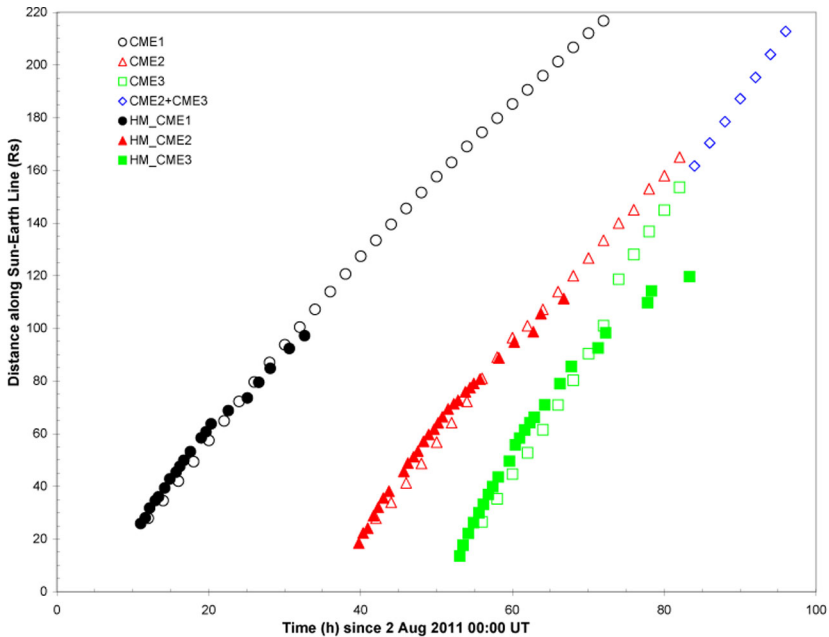
Figure 14 Radial distances of the CMEs along the Sun–Earth line derived from the WSA–Enlil-cone simulations (open symbols) and the analytic harmonic mean (HM) approximation (filled symbols). For the WSA–Enlil-cone results, the ensemble cone members are the same as in Figures 9 and 13. For the HI-1 data points shown between 0 $R_\odot$ and 80 $R_\odot$, the error bars are ± 1.6 for CME1, ± 1.1 for CME2, and ± 1.3 for CME3. For the HI-2 data points shown after 80 $R_\odot$, the error bars are ± 6.8 for CME1, ± 5.5 for CME2, and ± 3.0 for CME3. These errors are based on the estimated uncertainties in the elongation measurements of $\pm 0.25°$ for HI-1 and $\pm 0.85°$ for HI-2 (due to the lower spatial and temporal resolution), as well as the uncertainty in the CME direction of $\pm 5.0°$.

and is attributed to our visual identification of the density peaks along the Sun–Earth line in the CME density profiles plots (not shown) that are similar to those shown in Figure 12 for the CME speed profiles. When the individual CMEs propagate through the solar wind, the position of highest density for each CME occurs at the top of the density curve that is shaped more or less like a bell curve. When the CME3 leading-edge front initially encounters the trailing edge of CME2, however, the CME3 density curve no longer maintains a bell shape and the highest density value occurs at the compression region of the distorted density curve. Given the numerical-grid resolution that is used for our simulations, the transition of the peak-density position from the top of a bell-shape curve to the top of the compression region of a distorted curve occurs in one numerical time-step. Hence, the unphysical "sudden acceleration" between two data points is seen (between 100 $R_\odot$ to 120 $R_\odot$) for the WSA–Enlil-cone CME3 results. As CME3 continues to merge into CME2, the density curve regains a bell shape. At around 165 $R_\odot$, both CME2 and CME3 merge (open-diamonds in blue).

Despite the small differences, the numerical results of CME radial distances derived using WSA–Enlil cone are very similar to those that are calculated from the HM approximation, which is a very different, independent methodology that uses spacecraft measurements of the CME elongation angles. The comparable agreement between the two methods supports our selection of the input DU map as well as the cone parameters and their combinations for CMEs 1, 2, and 3. It should be noted that the HM methodology was developed as a tool for better understanding CME dynamics from SECCHI observations (Lugaz, Vourlidas,

and Roussev, 2009) and is meant to be used together with 3D-fitting methods and numerical simulations of CME events. Since only a few modeling studies have provided such a comparison, especially for a succession of CME events (*e.g.* Lugaz, Vourlidas, and Roussev, 2009; Webb *et al.*, 2009), the results presented above will provide useful feedback to the developers of the HM methodology. Moreover, the qualitative comparison provides one example for model users on how the radial distances calculated from each method can be used together with figures such as Figures 9 and 13 for analyzing CME events, particular those that involve interacting CMEs. A detailed analysis of the interactions between CME2 and CME3 will not be presented here, since it is beyond the scope of this article.

7. Concluding Remarks

We demonstrated in this study the capability of the WSA–Enlil-cone modeling system in simulating a succession of three halo CME events that occurred in August 2011. By conducting an ensemble modeling study, we explored how different factors may affect the simulation results and to what extent the variations in the modeling parameters affect the accuracy in the simulation results, such as the CME arrival time. Our modeling ensemble included small variations to the input cone parameters (*e.g.* cone angular width) and the use of different input synoptic photospheric magnetic-field maps to drive the background solar wind. We also explored how the inclusion or exclusion of one or two of the preceding CMEs affect the solar-wind conditions through which the succeeding CME propagates. As expected, the best modeling ensemble is obtained when all three CMEs are included in a single simulation run. However, we emphasize that it is a combination of using the best-fit cone parameters and their combinations for all three CMEs, and having an accurate description of the pre-event background solar wind that play a large role in producing good modeling results. Consistent with the results from our previous study (Lee *et al.*, 2013b), the accuracy of the background, which depends on the reliability of the input DU map, has a stronger effect on the accuracy of the modeling results than the small variations in the cone parameters for each CME.

Although we found that including previous CMEs in a multi-CME event can have a strong effect on the accuracy of the arrival-time predictions even when there is no direct interaction between the CMEs, this result is specific to our case study. Thus further studies are needed to determine whether improvements in the modeled arrival times will always occur when prior CMEs are included in multi-event simulations. Such studies will be useful to the scientific and space-weather forecasting communities for determining the level of importance in taking into account CME events from the past several days.

In practice, the ensemble modeling of a multi-CME event in real-time would involve a larger set of simulations since one would not be able to select the best-fit cone parameters, such as for CME1 and CME2 from our case study, and would need to consider all cone parameters for each CME. As such, the real-time ensemble results would show the spreads for CME1 and CME2 in the modeling of CME1+CME2+CME3 (*e.g.* Figure 11) and may alter the conclusions regarding the spreads in the modeled arrival times in the different multi-CME simulation scenarios.

Finally, we remark that even though there is a lack of magnetic-cloud and flux-rope information in the CMEs, we showed that the WSA–Enlil-cone modeling system can be successfully used to simulate and study a succession of CME events.

8. Disclosure of Potential Conflicts of Interest

The authors declare that they have no conflict of interest.

References

Arge, C.N., Pizzo, V.J.: 2000, Improvement in the prediction of solar wind conditions using near-real time solar magnetic field updates. *J. Geophys. Res.* **105**, 10465.

Arge, C.N., Odstrcil, D., Pizzo, V.J., Mayer, L.R.: 2003, Improved method for specifying solar wind speed near the Sun. In: Velli, M., Bruno, R., Malara, F., Bucci, B. (eds.) *Tenth Internat. Solar Wind Conf.* **CS-679**, AIP, Melville, 190.

Arge, C.N., Luhmann, J.G., Odstrcil, D., Schrijver, C.J., Li, Y.: 2004, Stream structure and coronal sources of the solar wind during the May 12th, 1997 CME. *J. Atmos. Solar-Terr. Phys.* **66**, 1295.

Arge, C.N., Henney, C.J., Koller, J., Compeau, C.R., Young, S., MacKenzie, D., Fay, A., Harvey, J.W.: 2010, Air force data assimilative photospheric flux transport (ADAPT) model. In: Maksimovic, M., Issautier, K., Meyer-Vernet, N., Moncuquet, M., Pantellini, F. (eds.) *Twelfth Internat. Solar Wind Conf.* **CP-1216**, AIP, Melville, 343. DOI.

Arge, C.N., Henney, C.J., Koller, J., Toussaint, W.A., Harvey, J.W., Young, S.: 2011, Improving data drivers for coronal and solar wind models. In: Pogorelov, N.V., Audit, E., Zank, G.P. (eds.) *5th Internat. Conf. Numerical Modeling of Space Plasma Flows*, *ASTRONUM-2010* **444**, Astron. Soc. Pac., San Francisco, 99.

Brueckner, G.E., Howard, R.A., Koomen, M.J., Korendyke, C.M., Michels, D.J., Moses, J.D., Socker, D.G., Dere, K.P., Lamy, P.L., Llebaria, A., Bout, M.V., Schwenn, R., Simnett, G.M., Bedford, D.K., Eyles, C.J.: 1995, The Large Angle Spectroscopic Coronagraph (LASCO). *Solar Phys.* **162**, 357. ADS, DOI.

Burlaga, L.F., Plunkett, S.P., St. Cyr, O.C.: 2002, Successive CMEs and complex ejecta. *J. Geophys. Res.* **107**(A10), 1266. DOI.

Davies, J.A., Harrison, R.A., Rouillard, A.P., Sheeley, N.R., Perry, C.H., Bewsher, D., Davis, C.J., Eyles, C.J., Crothers, S.R., Brown, D.S.: 2009, A synoptic view of solar transient evolution in the inner heliosphere using the heliospheric imagers on STEREO. *Geophys. Res. Lett.* **36**, L02102. DOI.

Farrugia, C.J., Jordanova, V.K., Thomsen, M.F., Lu, G., Cowley, S.W.H., Ogilvie, K.W.: 2006, A two-ejecta event associated with a two-step geomagnetic storm. *J. Geophys. Res.* **111**, A11104. DOI.

Gopalswamy, N., Yashiro, S., Michalek, G., Kaiser, M.L., Howard, R.A., Reames, D.V., Leske, R., von Rosenvinge, T.: 2002, Interacting coronal mass ejections and solar energetic particles. *Astrophys. J. Lett.* **572**, L103.

Harvey, J.W., Hill, F., Hubbard, H.P., Kennedy, J.R., Leibacher, J.W., Pintar, J.A., Gilman, P.A., Noyes, R.W., Title, A.M., Toomre, J., *et al.*: 1996, The Global Oscillation Network Group (GONG) project. *Science* **272**, 1284.

Henney, C.J., Toussaint, W.A., White, S.M., Arge, C.N.: 2012, Forecasting F10.7 with solar magnetic flux transport modeling. *Space Weather* **10**, S02011. DOI.

Howard, R.A., Moses, J.D., Socker, D.G., Dere, K.P., Cook, J.W.: 2002, Sun Earth Connection Coronal and Heliospheric Investigation (SECCHI). *Adv. Space Res.* **29**, 2017.

Kaiser, M.: 2005, The STEREO mission: An overview. *Adv. Space Res.* **36**, 1483.

Lee, C.O., Arge, C.N., Odstrcil, D., Millward, G., Pizzo, V.: 2013a, Ensemble modeling of successive halo CMEs observed during 2–4 Aug 2011. In: Zank, G.P., Borovsky, J., Bruno, R., Cirtain, J., Cranmer, S., Elliot, H., Giacalone, J., Gonzalez, W., Li, G., Marsch, E., Moebius, E., Pogorelov, N., Spann, J., Verkhoglyadova, O. (eds.) *Thirteenth Internat. Solar Wind Conf.* **CP-1539**, AIP, Melville, 223. DOI.

Lee, C.O., Arge, C.N., Odstrcil, D., Millward, G., Pizzo, V., Quinn, J.M., Henney, C.J.: 2013b, Ensemble modeling of CME propagation. *Solar Phys.* **285**, 349. DOI.

Liu, Y., Luhmann, J.G., Möstl, C., Martinez-Oliveros, J.C., Bale, S.D., Lin, R.P., Harrison, R.A., Temmer, M., Webb, D.F., Odstrcil, D.: 2012, Interactions between coronal mass ejections viewed in coordinated imaging and in situ observations. *Astrophys. J. Lett.* **746**, L15.

Lugaz, N., Manchester, W.B. IV, Gombosi, T.I.: 2005, Numerical simulation of the interaction of two coronal mass ejections from the Sun to Earth. *Astrophys. J.* **634**, 651.

Lugaz, N., Roussev, I.I., Vourlidas, A.: 2009, Large-scale structures caused by interacting coronal mass ejections: Their formation and detection as revealed by MHD simulations. *Geophys. Res. Abstr.* **11**, EGU General Assembly 2009, Abstract 6510.

Lugaz, N., Vourlidas, A., Roussev, I.I.: 2009, Deriving the radial distances of wide coronal mass ejections from elongation measurements in the heliosphere – Application to CME–CME interaction. *Ann. Geophys.* **27**, 3479.

Lugaz, N., Vourlidas, A., Roussev, I.I., Jacobs, C., Manchester, W.B. IV Cohen, O.: 2008, The brightness of density structures at large solar elongation angles: What is being observed by STEREO SECCHI? *Astrophys. J. Lett.* **684**, L111.

Martinez-Oliveros, J.C., Raftery, C.L., Bain, H.M., Liu, Y., Krupar, V., Bale, S., Krucker, S.: 2012, The 2010 August 1 Type II burst: A cme–cme interaction and its radio and white-light manifestations. *Astrophys. J.* **748**, 66.

Millward, G., Biesecker, D., Pizzo, V., de Koning, C.A.: 2013, An operational software tool for analysis of coronagraph images: Determining CME parameters for input into the WSA–Enlil heliospheric model. *Space Weather* **11**, 57. DOI.

Möstl, C., Davies, J.A.: 2013, Speeds and arrival times of solar transients approximated by self-similar expanding circular fronts. *Solar Phys.* **285**, 411. ADS, DOI.

Möstl, C., Farrugia, C.J., Kilpua, E.K.J., Jian, L.K., Liu, Y., Eastwood, J.P., Harrison, R.A., Webb, D.F., Temmer, M., Odstrcil, D., et al.: 2012, Multi-point shock and flux rope analysis of multiple interplanetary coronal mass ejections around 2010 August 1 in the inner heliosphere. *Astrophys. J.* **758**. DOI.

Odstrcil, D.: 2003, Modeling 3D solar wind structure. *Adv. Space Res.* **32**, 497.

Shen, F., Feng, X.S., Wang, Y., Wu, S.T., Song, W.B., Guo, J.P., Zhou, Y.F.: 2011, Three-dimensional MHD simulation of two coronal mass ejections' propagation and interaction using a successive magnetized plasma blobs model. *J. Geophys. Res.* **116**, A09103. DOI.

Temmer, M., Vrsnak, B., Rollett, T., Bein, B., de Koning, C.A., Liu, Y., Bosman, E., Davies, J.A., Möstl, C., Zic, T., Veronig, A.M., *et al.*: 2012, Characteristics of kinematics of a coronal mass ejection during the 2010 August 1 CME-CME interaction event. *Astrophys. J.* **749**, 57.

Webb, D.F., Howard, T.A., Fry, C.D., Kuchar, T.A., Odstrcil, D., Jackson, B.V., Bisi, M.M., Harrison, R.A., Morrill, J.S., Howard, R.A., Johnston, J.C.: 2009, Study of CME propagation in the inner heliosphere: SOHO LASCO, SMEI, and STEREO HI observations of the January 2007 events. *Solar Phys.* **256**, 239. ADS, DOI.

Xie, H., Ofman, L., Lawrence, G.: 2004, Cone model for halo CMEs: Application to space weather forecasting. *J. Geophys. Res.* **109**, A03019. DOI.

Zhao, X.P., Plunkett, S.P., Liu, W.: 2002, Determination of geometrical and kinematical properties of halo coronal mass ejections using the cone model. *J. Geophys. Res.* **107**, CiteID 1223, SSH 13-1. DOI.